The Effect of Vertical Wind Shear on Radiative–Convective Equilibrium States

Françoise R. Robe and Kerry A. Emanuel

Program in Atmospheres, Oceans, and Climate, Massachusetts Institute of Technology, Cambridge, Massachusetts

ABSTRACT

Using a three-dimensional cloud ensemble model, a systematic exploration is undertaken of radiative–convective equilibrium states as a function of the structure and magnitude of an imposed background flow with vertical shear. In such simulations, mesoscale organization appears naturally, independent of the particulars of the initial condition. As the magnitude of an imposed low-level shear increases, the convection becomes increasingly organized in lines or arcs, propagating broadly downshear, as predicted by earlier work. When the shear is very strong, the convection tends to organize into lines at an angle to the shear, such that the line-normal component is not far from its theoretical optimal value. Midlevel shear favors shear-parallel lines, but if it occurs in conjunction with sufficiently strong low-level shear, the convection can become very strongly organized into lines or arcs generally orthogonal to the low-level shear. Optimal organization occurs when the depth of the shear layer is comparable to that of the cold pools associated with the convective downdrafts.

As the vertical shear is increased, the domain-averaged convective available potential energy (CAPE) at first increases but then decreases at stronger shear values. Associated with these changes, the lower to middle troposphere becomes drier at low shear values and more humid when the shear is strong. This relationship between humidity and CAPE is broadly consistent with recently developed CAPE theories. The authors also confirm previous work that shows that the transport of momentum by the simulated convection, though usually down the gradient of the background flow, is nonlocal in character.

Finally, some simulations are performed with an imposed hodograph taken from a tropical cyclone. Convective arcs form with an orientation similar to observed outer spiral bands, but the simulated bands propagate more rapidly than observed, perhaps because of a dry middle troposphere in the simulations.

1. Introduction

Deep convection often occurs in the form of squall lines or arcs. In the last two decades or so, it has become generally accepted that organization of convection into lines is usually a consequence of the interaction between the density currents produced by evaporation of rain and the low-level vertical shear of the environmental flow (Thorpe et al. 1982, hereafter TMM; Rotunno et al. 1988, hereafter RKW). According to these theories, convergence is enhanced on the downshear side of the cold pools, and the convection generated there is more likely to be upright, leading to squall lines that propagate preferentially downshear. For a particular thermodynamic state, there is a particular value of the shear that gives the most robust squall line; we shall hereafter refer to this value as the optimal shear. These theories have received some support from simulations with cloud-resolving, nonhydrostatic models. Many of these (e.g., Takeda 1971; Hane 1973; Schlesinger 1973; TMM; Yoshizaki 1986; Dudhia et al. 1987; Nicholls 1987; LaFore and Moncrieff 1989; Fovell and Ogura 1988,

1989) are two-dimensional, so that the orientation of the squall line is preordained. Most of the three-dimensional simulations (e.g., RKW; Nicholls and Weisbluth 1988; Weisman 1993; Skamarock et al. 1994; Trier et al. 1997) are designed to investigate the detailed structure and evolution of the convection, and so do not generally integrate long enough to become independent of their initial condition; moreover, these simulations are unforced, so that long-term equilibrium cannot be achieved.

Our intent, by contrast, is to examine in some detail the effect of vertical shear on the general characteristics of statistical equilibrium states of convection, and we take radiative–convective equilibrium to be the simplest of such states. We wish to understand the effect of the shear on the thermodynamic properties of the equilibrium state as well as on the structure and intensity of the convection, in a system with a very limited number of externally specified control parameters. While being aware that real convection generally occurs in environments that are perturbed away from radiative–convective equilibrium by the presence of large-scale circulations, we hope to understand some of the basic physics underlying the interaction between convection and shear in system with a manageable number of external control variables.

Corresponding author address: Dr. Kerry A. Emanuel, Rm. 54-1620, MIT, 77 Mass. Ave., Cambridge, MA 02139.
E-mail: emanuel@texmex.mit.edu

Several three-dimensional ensemble convective simulations of radiative–convective equilibrium states have been performed in the last decade, beginning with the work of Islam (1991) and Islam et al. (1993). In these simulations, the radiative cooling of the troposphere is specified and the surface fluxes are calculated using bulk aerodynamics formulas. Among the significant conclusions of this work are that (a) starting from an arbitrary initial state, statistical equilibrium is achieved in roughly 3 days; (b) the spatial distribution of convection is more nearly regular than random, showing that cells are less likely to form adjacent to each other than far apart; and (c) to achieve the same statistical stability with a two-dimensional model, about as many grid points are needed as with a three-dimensional model, showing that for equilibrium ensemble calculations there is little or no cost saving from using two-dimensional models. Robe and Emanuel (1996, hereafter RE) showed, in addition, that increasing the imposed rate of radiative cooling increases the convective mass flux not by increasing the buoyancy or vertical velocity of updrafts but by increasing their fractional area. Remarkably, there is little change in either the ensemble-averaged CAPE or the vertical profile of relative humidity as the rate of cooling is changed. Emanuel and Bister (1996) attempted to explain the independence of the cloud velocity scales on the rate of forcing using an entropy-based argument.

The studies cited above did not impose any large-scale environmental flow in their doubly periodic domains (though we note that horizontally domain-averaged flows could have, but did not, result from the convection itself). In the three-dimensional radiative–convective simulations by Vallis et al. (1997), a uniform background flow was imposed, resulting in some vertical shear in a turbulent boundary layer. Deep convection in their simulations was organized into arcs broadly orthogonal to the boundary layer shear, whether or not a Coriolis parameter was included. Vallis et al. (1997) focused on the energetics and nature of the turbulent cascade in their simulations and did not explore sensitivity to background shear. Our simulations are very similar to those of Vallis et al., but we do not include a Coriolis parameter and focus instead on the effect of imposed shear on the structure and intensity of the convection, and on the thermodynamic characteristics of the environment. The design of the model is briefly reviewed in the following section. In section 3 we describe the results of simulations with an imposed constant vertical shear in the first few kilometers, while in section 4 the results of adding shear above the boundary layer are presented. Simulations using an observed hodograph from the outer region of a tropical cyclone are discussed in section 5, and a summary is presented in section 6.

2. Model and experimental design

We used version 3.1 of the Advanced Regional Prediction System model designed by Xue, Droegmeier, and associates at the Center for Analysis and Prediction of Storms, as described by Xue et al. (1993), with modifications described in Robe and Emanuel (1996), which should be consulted for a detailed description of the model setup. The model is fully compressible and non-hydrostatic and is run on a doubly periodic domain of 180 km $\times$ 180 km extending from the surface to an altitude of 19 km. A sponge layer extends from 15.5 to 19 km, with a relaxation time of 100 s. Uniform spatial resolution of 2 km in the horizontal and 500 m in the vertical is used. Subgrid-scale mixing is represented using a Richardson-number-dependent Smagorinsky scheme. As such a scheme produces virtually no diffusion over the large fractions of the domain that are stable, it is necessary to add more diffusion to stabilize the numerical integration. In an attempt to minimize the physical effects of such diffusion, we used fourth-order diffusion with a horizontal coefficient of 6×10^7 m^4 s^{-1} and a vertical coefficient of 2.5×10^5 m^4 s^{-1}. Surface heat and moisture fluxes are represented using bulk aerodynamic formulas with a background wind speed of 10 m s^{-1}. This relatively large value is motivated by the need for large surface enthalpy fluxes to compensate the relatively large, imposed radiative cooling discussed presently. The surface is taken to be an ocean with a fixed temperature of 300 K. No surface drag is included in the model. The microphysics is represented according to the scheme of Kessler (1969), which does not include the ice phase. However, to prevent saturation of the upper troposphere, we modified the autoconversion threshold liquid water content to vary linearly with temperature from its standard value above 0°C to zero at −20°C. Such a variation was found by Emanuel and Zivkovic-Rothman (1999) to give an accurate prediction of relative humidity in the upper troposphere in a single-column model forced by data collected during the Tropical Ocean Global Atmosphere Coupled Ocean–Atmosphere Response Experiment. We also modified the model to conserve water precisely by ''borrowing'' water substance from adjacent grid points in rectifying negative specific humidities.

The model is forced by a specified, constant radiative cooling rate from the surface up to 13 km. While this prevents possible instabilities that rely on feedbacks between radiation and clouds and water vapor, it greatly simplifies the computations and their interpretation. We also performed an experiment in which the fixed rate of cooling was replaced by radiation calculated at the top of the atmosphere using the simplified scheme of Thompson and Warren (1982), which allows for the dependence of radiation on temperature, humidity, and cloud properties. The divergence of the radiative flux was specified to be constant through the troposphere, so that the radiative cooling is constant with height (but variable in horizontal space and time) up to 13 km. The results of this experiment were nearly indistinguishable from those using the specified rate of cooling. In the experiments presented in this paper, the rate of cooling

was 5.4 K day^{-1}, which is somewhat larger than observed in nature but greatly accelerates the approach to statistical equilibrium.

The model is initialized by first specifying the vertical profiles of temperature and specific humidity from the Atlantic hurricane season mean sounding of Jordan (1958). To initiate convection, spatially random temperature perturbations, ranging from −0.2 to 0.2 K with zero mean are maintained for the first 30 min of integration. The model is then run into a state of statistical equilibrium, which usually takes several days (Robe and Emanuel 1996). To save time, the model is first run on a 60 km × 60 km domain for 138 h, and then the doubly periodic domain is unfolded to 180 km × 180 km and the integration is continued.

At 138 h, a horizontally uniform but vertically varying background wind is added to the domain. If this background wind is not artificially maintained, we observe that in the experiments, it decays roughly exponentially with a timescale of around 12 h, owing to convective momentum transport. [This is also consistent with estimates of convective damping of shear made by Mapes and Wu (2001).] The interaction between convection and large-scale flows does not, in this model, lead to maintenance of those flows, as sometimes happens in laboratory convection. As there are no large-scale pressure gradients or Coriolis accelerations in the model, we must maintain the shear artificially. To do so, we simply restore the horizontally averaged flow at each level every time step, by adding an appropriate constant vector at each level. This does not affect the divergence or vorticity of the flow and so has no direct effect on the convection. By keeping track of the momentum added to each model level every time step, we can diagnose the cumulus momentum flux averaged horizontally at each level in the statistical equilibrium state. An example of these diagnosed fluxes will be presented in the next section.

Apart from the addition of a background wind, the model is identical to that discussed by Robe and Emanuel (1996).

3. Effect of low-level shear

a. Convective organization and propagation

We first explore the effects of imposing a single layer of unidirectional shear adjacent to the surface, as in the experiments of RKW and Fovell and Ogura (1989). The shear in the wind U is characterized by an intensity S and a thickness H, as shown in Fig. 1. We explore the sensitivity of the radiative–convective equilibrium state to S and H and then to the product $\Delta U = S \times H$. A summary of the experiments is given in Table 1.

In the first set of experiments, the shear intensity is increased while the depth of the shear layer is held fixed at 2 km. Representative snapshots of the vertical velocity at 250 m are shown in Fig. 2 for each of the
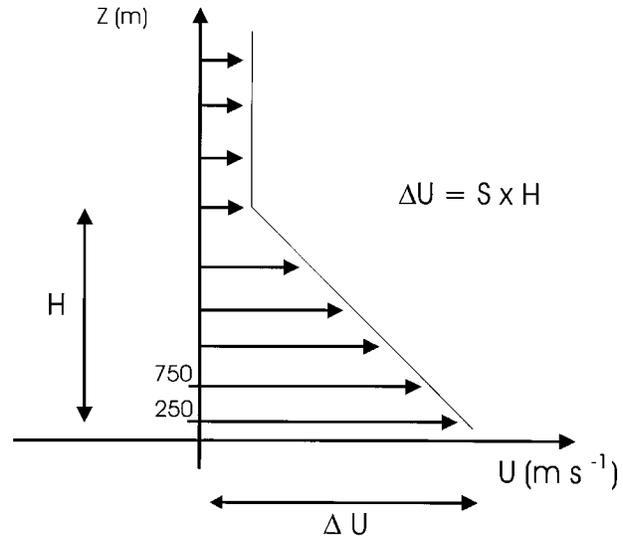

FIG. 1. Background flow for the unidirectional shear experiments. The magnitude of the shear is ΔU, occupying a depth H.

simulations. The numbers in parentheses at the bottom of each panel in Fig. 2 show an estimate of the lifetime of the particular mesoscale squall line or arc, made by tracking the feature subjectively in time. The surface cold pools associated with each of the frames in Fig. 2 are depicted in Fig. 3.

Without shear (Fig. 2a) the convection is more or less randomly organized, though as shown for a similar simulation by Islam et al. (1993), the distribution of convection is more nearly regular than random. On rare occasions, and for short times, the convection appears to be organized in closed circles or ellipses, along the boundaries of spreading cold pools (see Fig. 3b).

As the magnitude of the shear (which is from right to left in the figures) is increased, the convection becomes increasingly organized into arcs, broadly perpendicular to the shear; but for very strong shear [I8 (not shown) and I10], there is an apparent preference for lines at some angle to the shear. The longevity of the lines at first increases with the shear, but then decreases again for very strong shear, except for I8, which contains long-lived lines.

The temperature deficits in the cold pools in experiments I3 up through I6 are comparable, though the cold pool in I4 is somewhat weaker and does not have as sharp a gradient at its edge. The coldest surface air in the no-shear experiment (I0) is comparable to that of the low-shear experiments. The cold pools in the high-shear runs (I7–I10) are much colder, reaching −5 K in I7 and I8 and −7 K in I10. Corresponding to this greater temperature deficit, the squall lines in the high-shear cases propagate faster, relative to the background flow, than those in the low-shear cases.

In an attempt to quantify the orientation and propagation of the squall lines, we subjectively estimated the background surface flow-relative propagation speed and

TABLE 1. Experiments with shear.

Type	Name	Shear intensity (S) $(10^{-3}$ s$^{-1})$	Thickness (H) (km)	Special features
Control	I0	0	0	No shear
Intensity	I3	3	2	
	I4	4	2	
	I5	5	2	
	I6	6	2	
	I7	7	2	
	I8	8	2	
	I10	10	2	
Thickness	3T1	3	1.5	
	3T2	3	2	
	3T3	3	3.5	
	4T1	4	2	
	4T2	4	2.5	
	5T1	5	1	
	5T2	5	2	
	5T3	5	2.5	
	5T4	5	4	
Constant ΔU $(= S \times H)$	6DU1	2	3	
	6DU2	3	2	
	10DU1	4	2.5	
	10DU2	5	2	
	12DU1	4	3	
	12DU2	6	2	
WISHE	W8	8	2	Fixed wind in surface fluxes

the average angle, α, between the line orientation and the shear vector for many squall lines in each experiment in which they were evident (When α is 90°, the lines are oriented perpendicular to the shear.) The definition of the orientation angle is difficult because the bands are curved and their shape varies with time. We determine the orientation angle at the place and time where the updrafts at 250 m reach their maximum magnitude. The propagation speed is defined to be in the direction orthogonal to the band when and where it is most intense. The results are summarized in Table 2. The orientation of the bands with respect to the shear does not seem to follow any rule for low shear values; however, there is a correlation between orientation and strength of the cold pool in particular, and between orientation and intensity in general. The cold pool in I5 is the coldest of all the low shear cases and the band develops at the greatest angle from the shear; the cold pool in I4 is the weakest and its angle with respect to the shear is the smallest. As the shear is further increased, the bands tend to rotate further away from orthogonal to the shear. As indicated in Table 2, there is a tendency for the squall lines to assume an angle that maintains a near equivalence of the propagation speed and the component of ΔU across the band. Examination of vertical cross sections across the bands (not shown) shows that the updrafts always tilt upshear, in contrast to squall lines in the high-shear cases examined by RKW, in which the lines did not have the freedom to rotate away from the shear vector.

In general, these results support the contention of Emanuel (1986) that as the magnitude of the shear becomes superoptimal, squall lines rotate away from the direction orthogonal to the shear so as to preserve a near optimal cross-line component of the shear. However, in these simulations, as in those of Fovell and Ogura (1989), it is evident that the optimal shear value is a moving target, as the cold pool intensity generally increases with the shear.

We performed a number of simulations in which the thickness of the shear layer is varied, as summarized in Table 1. In general, the most intense and long-lived squall lines occur when the thickness of the shear layer is 2 km, which is usually close to the depth of the cold pool. This finding is in agreement with RKW, who stressed that the optimal shear layer thickness must match that of the cold pool. Figure 4 shows representative snapshots of the vertical velocity field in experiments with shear layers of varying thickness. One notable feature of these results is that strong, deep shear layers tend to promote shear-parallel convection (e.g., experiment 5T4). The results of the simulations with moderate shear (5×10^{-3} s^{-1}) are summarized in Table 3, which has been constructed in the same way as Table 2. As the depth of the shear layer increases beyond its optimal value of 2 km, the lines become increasingly parallel to the shear and the cross-line ΔU and propagation speed both decrease, even though the temperature of the cold pools is actually decreasing (not shown). To emphasize that the depth of the shear layer is an important parameter in its own right, we ran pairs of experiments in which ΔU is held fixed while the shear and depth of the shear layer vary individually. The results are illustrated by Fig. 5. Clearly, the depth of the shear layer is influential, even when ΔU is held fixed.
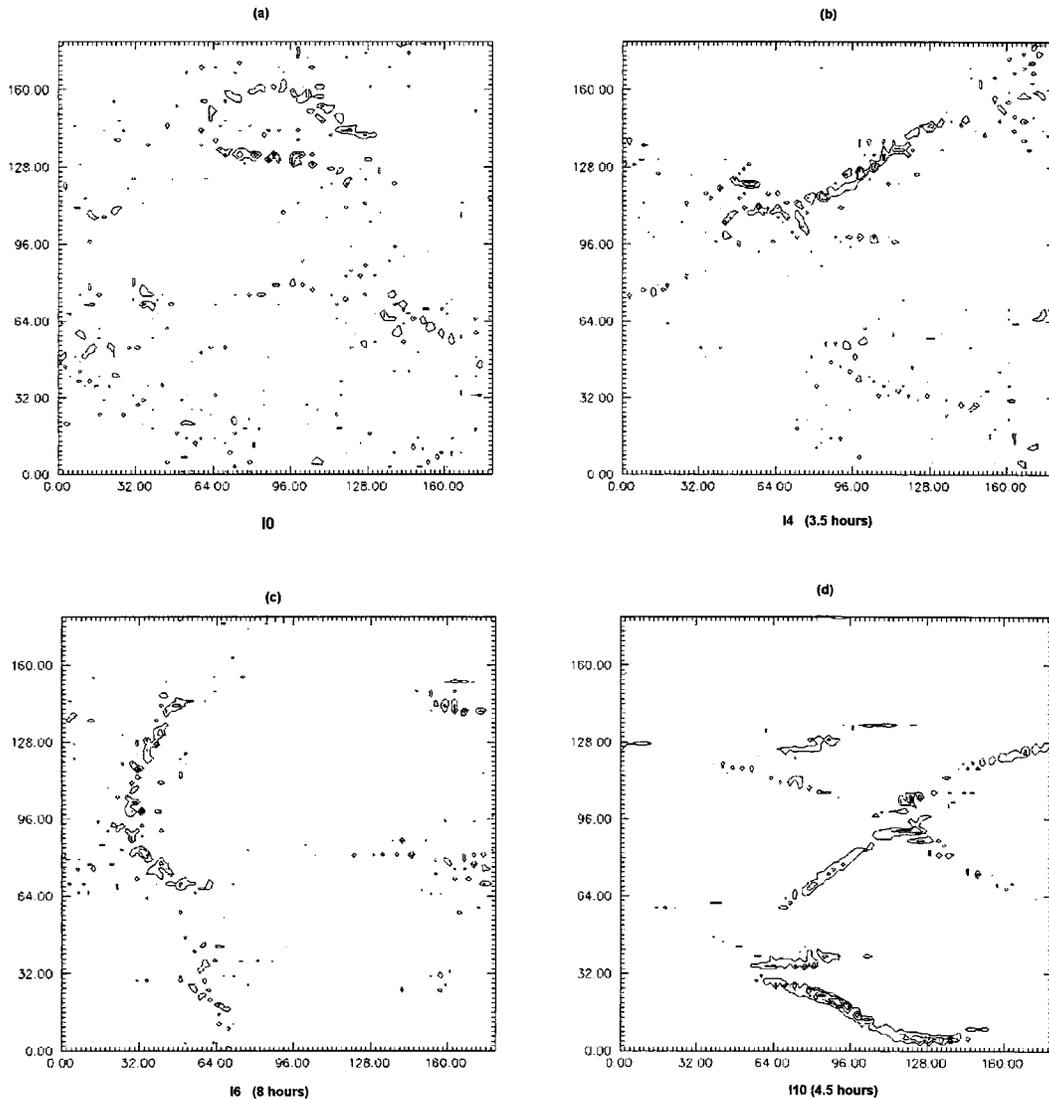
One issue that arises in many of these simulations is

FIG. 2. Updraft field at 250 m at selected times, as a function of the magnitude of the imposed background shear, ΔU: (a) 0; (b) 4 m s^{-1}; (c) 6 m s^{-1}; (d) 10 m s^{-1}. Typical lifetimes of the squall lines in each case are indicated by numbers in parentheses.

that when the convection is well organized, there is often only one squall line or arc in the domain at any given time. This suggests that the convection may be artificially limited by the finite size of the domain. Present computational limitations prevent us from exploring this issue further without degrading horizontal resolution, but future work of this nature should explore the use of larger domains.

b. Equilibrium thermodynamic state

The imposition of environmental shear also alters the thermodynamic structure of the radiative–convective equilibrium state. Changes in the temperature structure are subtle and we prefer to address changes in the convective available potential energy (CAPE). In Table 4

we list the domain-averaged CAPE also averaged over 12 h, as a function of the magnitude of the imposed low-level shear. Here CAPE is defined using reversible ascent from the lowest model level. (Although pseudoadiabatic ascent yields greater CAPE values, the relative change between experiments is the same.) As the shear increases, CAPE first increases but then decreases, reaching a minimum value when the largest shear is imposed. Figure 6 shows the domain-averaged relative humidity averaged between 12 and 24 h for all the experiments with low-level shear. Note that, as indicated in Table 4, the mean relative humidity from cloud base to 5 km is anticorrelated with changes in CAPE. This is in agreement with the expression for CAPE derived by Emanuel and Bister (1996):

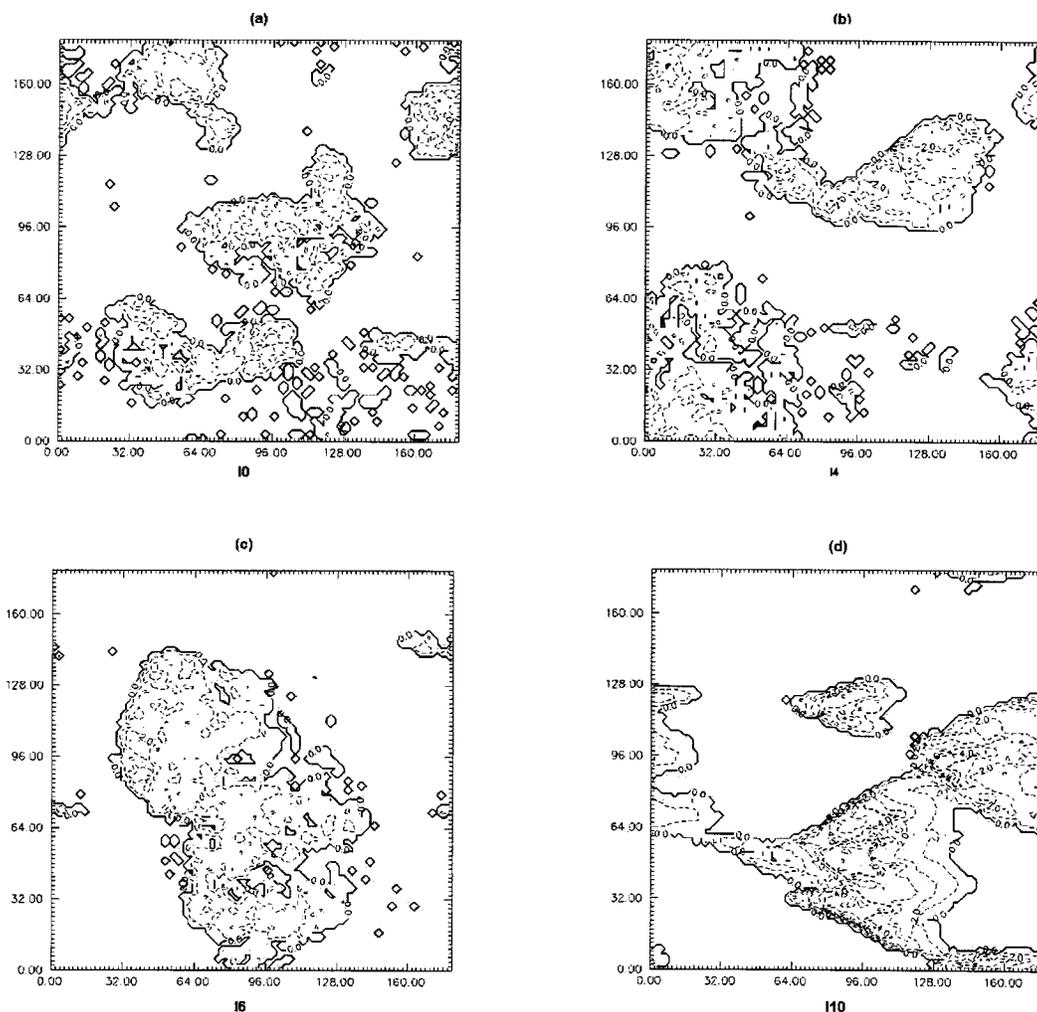$$\text{CAPE} = \varepsilon(h_b - h_m),$$

FIG. 3. Potential temperature perturbations (K) corresponding to the fields shown in Fig. 2. Contour interval is 1 K, and perturbations greater than −0.5 K have been set to zero.

where ε is a thermodynamic efficiency related to the mean temperatures at which radiation is absorbed and emitted, and h_b and h_m are the moist static energies of the boundary layer and the source region for downdraft air, respectively. Given that the surface fluxes are fixed in these experiments by the requirement that they balance the radiative cooling of the atmosphere, h_b is ef-

fectively fixed, while h_m varies with relative humidity. Thus, increasing the relative humidity of the low to middle troposphere should decrease CAPE, as indicated in Table 4.

On the other hand, it is not clear to us why the relative humidity changes the way it does in the simulations. We observe that in the very high shear cases, there are

TABLE 2. Band characteristics as a function of shear intensity.

Experiment	Shear intensity (S) (10^{-3} s^{-1})	Orientation angle (α)	Change in line-normal velocity across shear layer (m s^{-1})	Cold pool velocity relative to mean wind (m s^{-1})
I3	3	50°	4.5	8
I4	4	30°	4	7
I5	5	75°	9.5	11
I6	6	70°	11.5	6
I7	7	55°	11.5	11
I8	8	55°	13	12
I10	10	25°	8.5	10

(a)

5T1 (H=1 km; lifetime=3.5 h)

(b)

5T2 (H=2 km; lifetime=9 h)

(c)

5T3 (H=2.5 km; lifetime = 3 h)
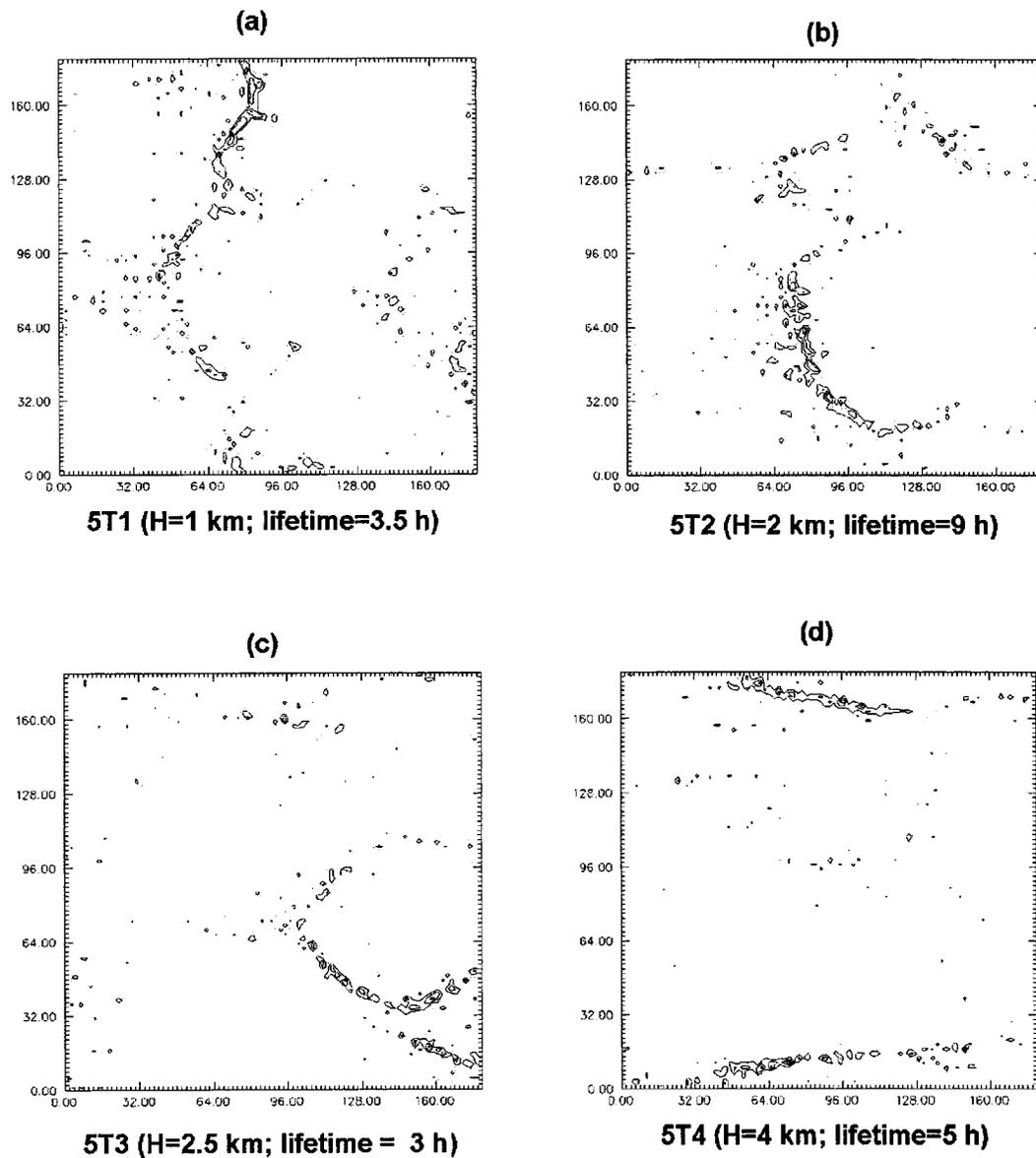
(d)

5T4 (H=4 km; lifetime=5 h)

FIG. 4. Updraft field at 250 m at selected times, as a function of the depth (*H*) of the imposed background shear. Shear depth and typical squall lifetimes are indicated below each panel.

numerous shallow cumuli, and the cold pools are particularly cold. It is also doubtful that the domain-averaged CAPE is a good measure of the buoyancy of updrafts, since the average itself is strongly influenced by the presence of the cold pools, which do not supply air to deep updrafts. A reviewer (B. Mapes) suggested that large shear may lead to mechanical turbulence in the lowest 2 km, giving rise to an artificially deep

TABLE 3. Band characteristics as a function of shear layer depth.

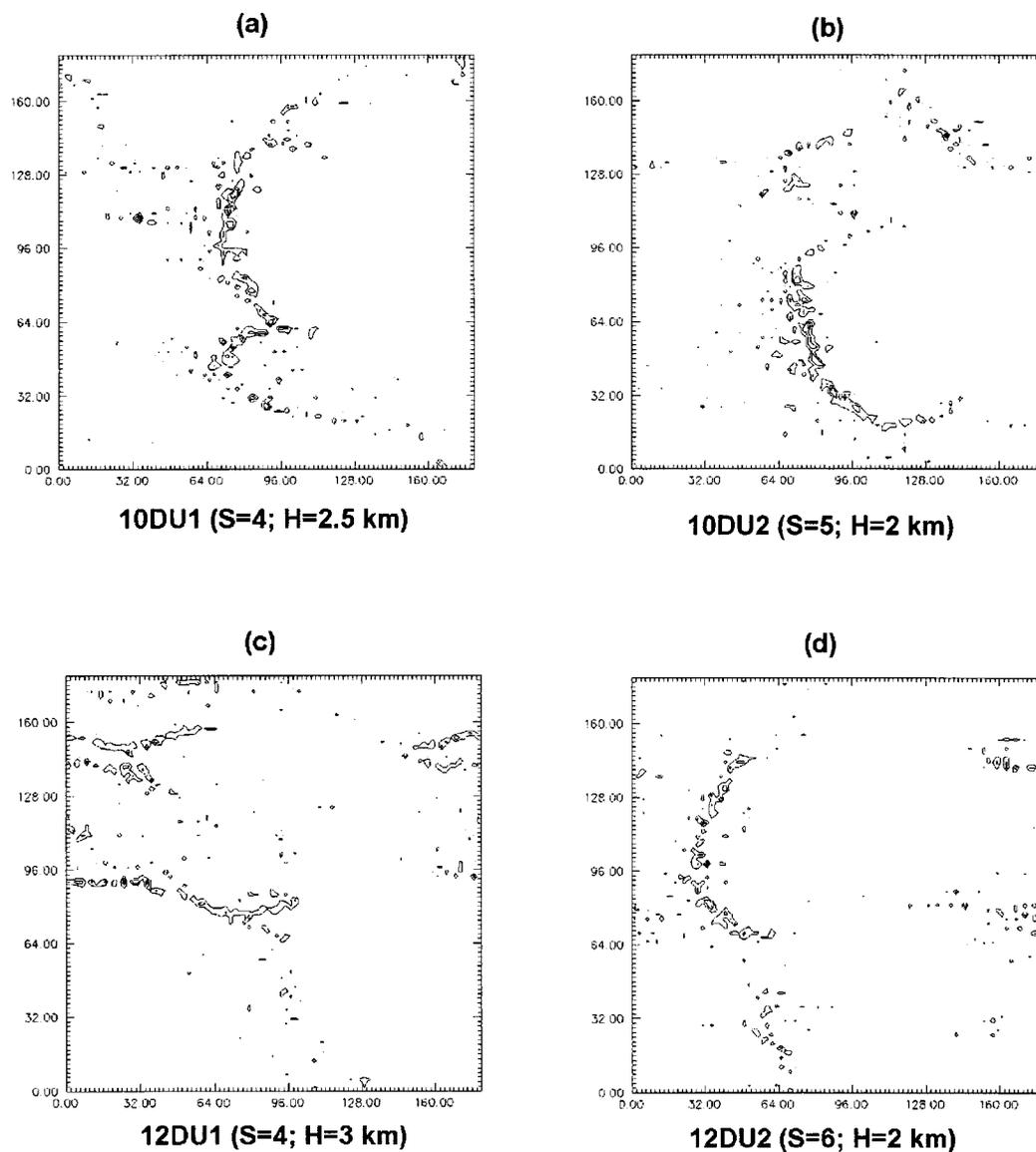| Experiment	Shear layer thickness (km)	Orientation angle (α)	Change in line-normal velocity across shear layer (m s^{-1})	Cold pool velocity relative to mean wind (m s^{-1})
5T1	1	55°	4	10
5T2	2	75°	9.5	11
5T3	2.5	35°	7	9
5T4	4	15°	5	8

FIG. 5. Updraft field at 250 m at selected times, in two pairs of experiments in which ΔU is fixed, in (a) and (b) at 10 m s^{-1}, and in (c) and (d) at 12 m s^{-1}. The magnitudes of the shear and depths of the shear layer are indicated below each panel.

TABLE 4. Equilibrium environmental characteristics as a function of shear intensity.

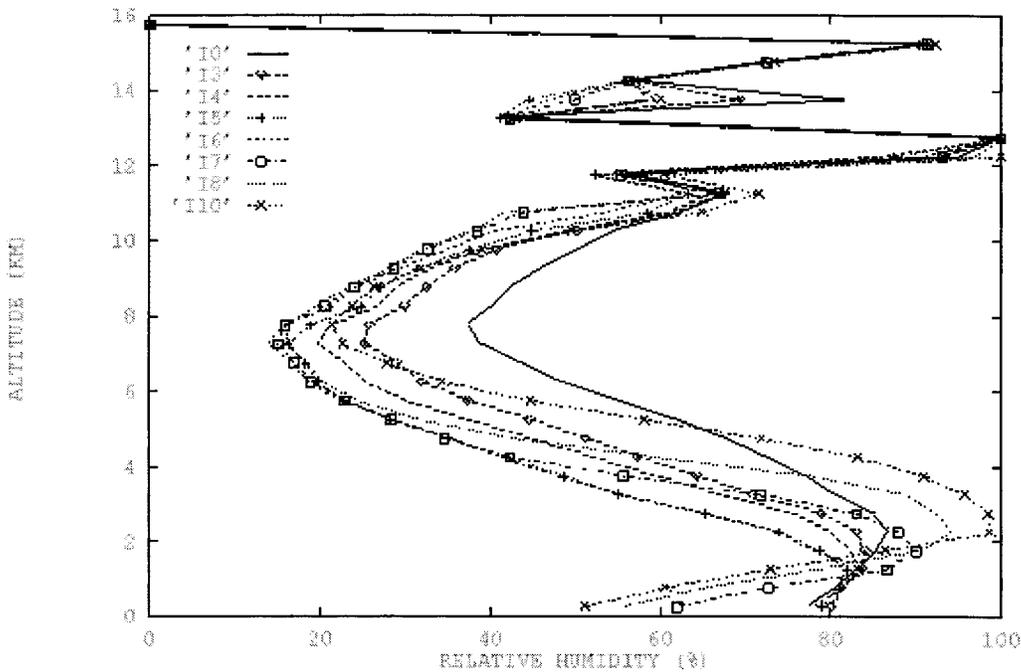| Experiment	Shear intensity (S) (10^{-3} s^{-1})	12-hour, domain-averaged CAPE (J Kg^{-1})	12-hour, 1–5-km mean relative humidity (%)
I0	0	930	77
I3	3	1350	68
I4	4	1430	64
I5	5	1400	58
I6	6	1470	58
I7	7	750	63
I8	8	600	70
I10	10	500	84

FIG. 6. Vertical profiles of the domain-averaged relative humidity averaged between 12 and 24 h in the experiments indicated in the upper left.

boundary layer with numerous shallow clouds and artificially depressed relative humidity and increased temperature near the surface, while at the same time elevating the humidity in the lower and middle troposphere. The plots of relative humidity suggest that as the shear increases, the boundary layer depth also increases discretely (jumping up model levels), leading to decreasing humidity at the surface.
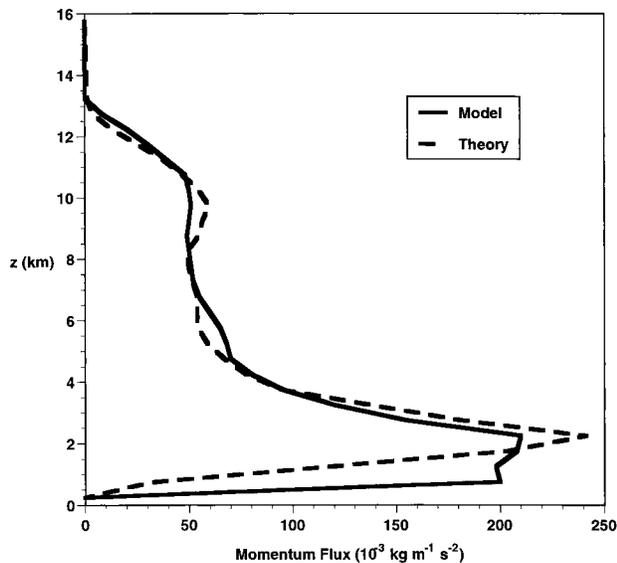

FIG. 7. Vertical convective momentum flux necessary to maintain background wind profile in the model (solid), and that deduced from equations (1) and (2) (dashed).

c. Momentum fluxes

Not only does convection control the temperature and moisture profiles in equilibrium, but it also transports momentum in the vertical. In these experiments, the background shear is maintained at every time step by adjusting the horizontally domain-averaged horizontal wind at each model level. By keeping track of the amount of momentum added, one may deduce the equilibrium vertical momentum transport by convection. This is shown for experiment I5 (Table 1) in Fig. 7. For comparison, we also show in Fig. 7 a simple estimate of the momentum flux given by

$$F = M(U_c - \overline{U}), \qquad (1)$$

where M is the updraft mass flux, U_c is a characteristic horizontal velocity within the updrafts, and $\overline{U}$ is the domain-averaged horizontal velocity. Here M is estimated as in Robe and Emanuel (1996) and is taken to be a horizontally domain-averaged value of the convective updraft mass flux. Schneider and Lindzen (1976) took U_c to be a constant representing the background horizontal wind at cloud base. We find that this gives serious overestimates of the convective fluxes in our simulations. We also tried several other formulations for the in-cloud velocity, including that of Kershaw and Gregory (1997). We found, however, that a particularly good fit is achieved by assuming that in-cloud horizontal velocity obeys a conventional aerodynamic drag law of the form

$$M\frac{\partial U_c}{\partial z} = -\lambda\rho(U_c - \overline{U})|U_c - \overline{U}|, \qquad (2)$$
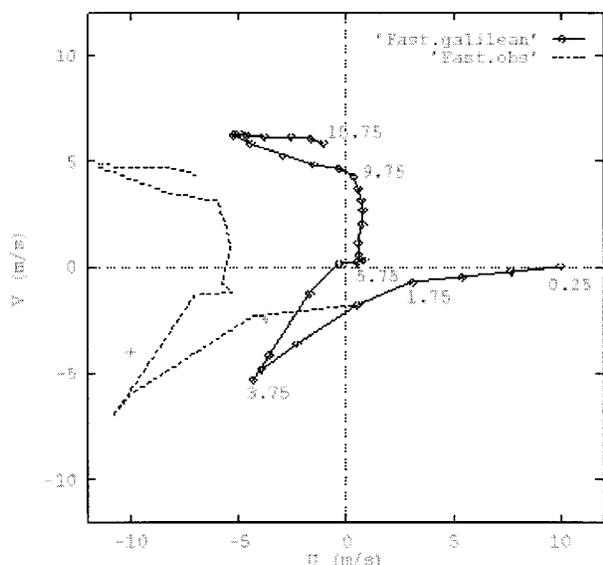
FIG. 8. The composite "fast" squall line hodograph deduced by Barnes and Sieckman (1984). The solid line represents the observed composite hodograph; the dashed line shows the hodograph after application of a Galilean transformation designed to keep the convection from propagating excessively fast through the domain.

where ρ is the air density and λ is a constant here taken to be $(250 \text{ km})^{-1}$. In solving (2), we take the starting value of U_c to be the value of the environmental wind at 0.25 km. This relation does surprisingly well, except just above cloud base, where it overestimates the momentum flux, and just below cloud base, where it is underestimated. It is possible that some of the momentum flux we ascribe to convection in the model is actually carried by the model's turbulence scheme in the boundary layer, where a shear is imposed but the stability is close to neutral. Both the model and the simple theory give downgradient momentum fluxes in the shear layer, but there is no gradient in the background flow above 2.25 km and yet there is substantial convective momentum flux, showing that the convective momentum flux is nonlocal, as are the enthalpy and water fluxes.

We stress that these results only apply to the particular shear profile we have discussed here. At the very least, it is likely that λ in (2) varies with the exact shape of the hodograph and with the component of horizontal momentum. Thus, for example, one would expect λ to be small for the along-line component of flow in shear-parallel convection.

4. Effects of shear above the boundary layer

In their analysis of tropical squall lines, Barnes and Sieckman (1984) noted that some of the lines were parallel to the shear while others were more nearly perpendicular. The composited wind profiles for these two classes of squall lines differ markedly: The shear in the parallel case is nearly unidirectional and extends

TABLE 5. Fast squall line experiments.

Name	Features
F0	Complete hodograph
F1	Low-level (0.25–1.75 km)
F2	Up to jet max (0.25–3.75 km)
F3	Through top of jet (0.25–5.75 km)
F4	To base of upper jet (0.25–9.75 km)

through a deep layer, while the shear-perpendicular lines occur in environments with strong low-level jets (having reversed shear above the jets). A composite hodograph in the environments of midlatitude continental squall lines (Wyss and Emanuel 1988) shows strong cross-line shear up to 4 km and moderate shear at about a 45° angle to the shear above 4 km.

To examine some of the effects of shear above the boundary layer, we first performed a number of experiments using the Barnes and Sieckman "fast" squall line composite hodograph, shown here in Fig. 8. While we use the observed composite wind profile, we do not impose the observed thermodynamic sounding, allowing the model to come into statistical equilibrium, as before. Our equilibrium sounding is somewhat moister than the composite Barnes and Sieckman sounding. To see the separate effects of various components of the shear in this hodograph, we ran a series of experiments as summarized in Table 5. The first of these (F0) uses the entire hodograph, while the others use progressively deeper segments of the hodograph. Representative snapshots of the vertical velocity at 250 m in these experiments are shown in Fig. 9.

When the full hodograph is used (F0), arcs of convection form, oriented broadly across the shear in the lowest 1.75 km, but with long, curved "tails." These propagate toward to east in the Galilean-shifted coordinate system at a speed of about 1 m s^{-1}, in contrast to the observed (transformed) speed of about 4.8 m s^{-1}. The slowness of our squall lines might result from the relatively moist sounding in these simulations, so that the outflow is not so cold and thus does not propagate rapidly. When only the lowest layer of shear is used (F1), the squall lines are oriented in about the same direction, but are weaker, which is not surprising in view of the relative weakness of the shear as well as thinness of the shear layer. These are "suboptimal" squall lines, in the terminology of RKW. Adding to this the strong shear layer up to the level of the jet (F2) dramatically alters the structure of the rainbands. The updrafts are more intense, but shorter lived than in F1, and their orientation is nearly parallel to the mean shear over the whole layer. When the reverse shear above the jet is added (F3), the orientation remains parallel to the low-level shear, but the squall lines are weaker than in F2, though of comparable duration and intensity to those in F1. The addition of mid- to upper-level shear (F4) once more completely changes the orientation of the bands. These bands are similar to those that develop in F0,

(a)

F0 (lifetime=7.25 h)

(b)

F1 (lifetime=5 h)

(c)

F2 (lifetime=3.25 h)

(d)

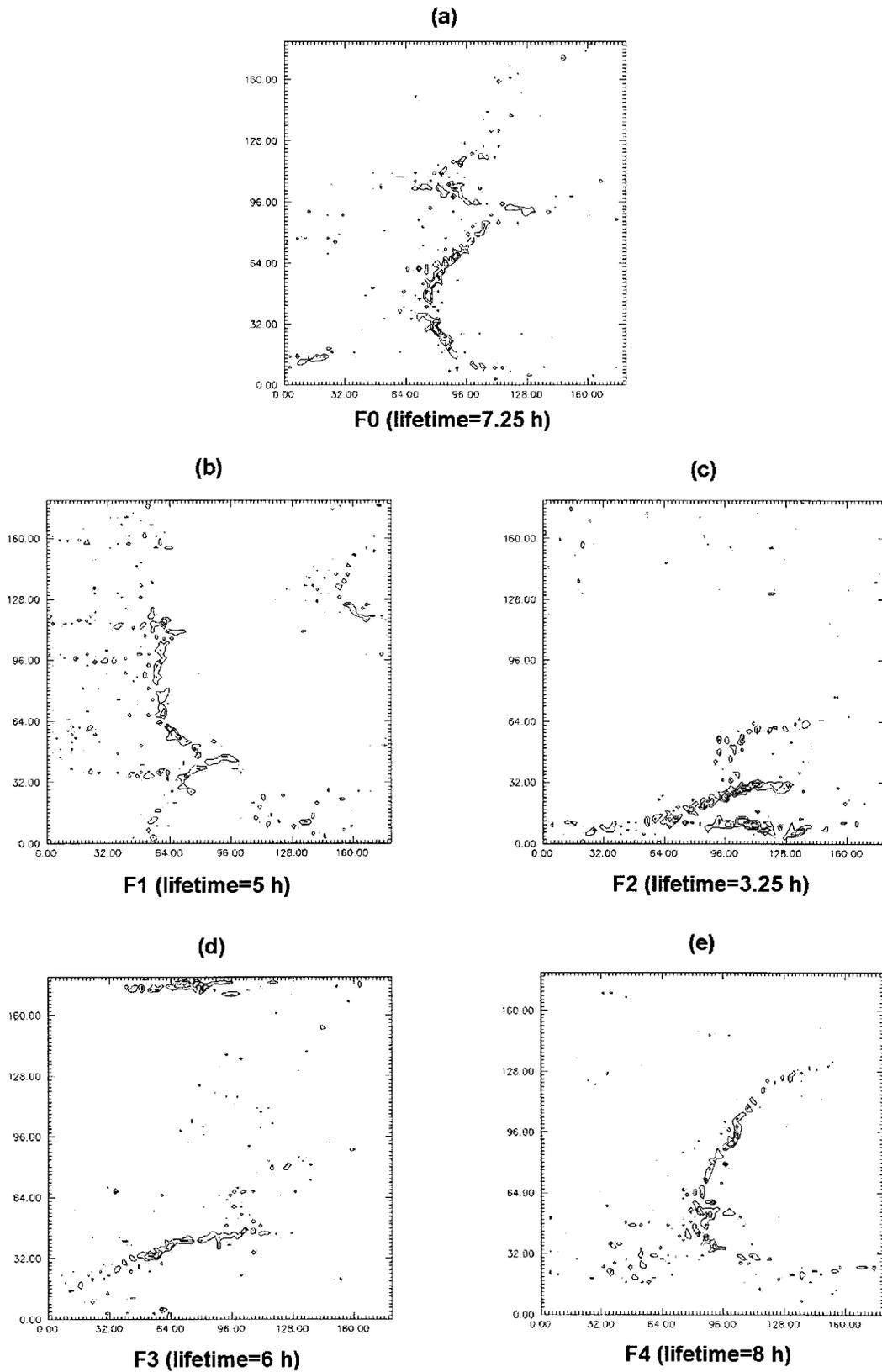**F3 (lifetime=6 h)**

(e)

F4 (lifetime=8 h)

Fig. 9. Updraft field at 250 m at selected times in experiments with the complete hodograph of Fig. 8, and with selected segments of the hodograph indicated in Table 5. Typical squall lifetimes are indicated at the bottom of each panel.
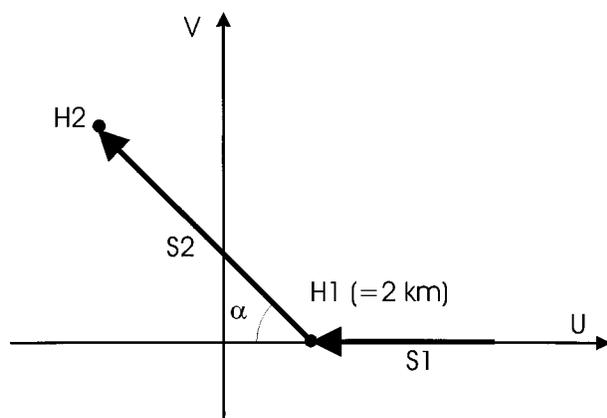
FIG. 10. Configuration of background flow in experiments with two layers of shear indicated by the vectors whose magnitudes are S1 and S2, the angle between which is α.

except that they form at slightly greater angle to the low-level shear. The F0 hodograph differs from that used in F4 in that it contains a high-level easterly jet. Examination of vertical cross sections of cloud water (not shown) reveals that this easterly jet forces the anvils to be more symmetric with respect to the updrafts; without the high-level jet, the anvil extends eastward from the updrafts and therefore drops more precipitation into the cold pools.

Clearly, the structure and propagation of convection

are affected by more than just the low-level shear. To better understand and quantify the effect of shear above the boundary layer, we undertake a series of experiments in which two layers of unidirectional shear are imposed, as illustrated in Fig. 10. The environmental hodograph is characterized by a set of five parameters: the intensity of the shear in each layer (S_1 and S_2), the thickness of each layer (H_1 and H_2), and the angle between the lower and upper shear vectors (α). We do not, however, vary the thickness of the lower layer. The set of experiments is described in Table 6. While these experiments do not explore the effect of shear in the high troposphere, they represent a systematic attempt to quantify and understand the effects of shear just above the boundary layer.

In the first set of experiments (33A in Table 6), the magnitude of the shear in the lower shear layer is less than its optimal value. The degree of organization into bands or arcs is weak, except when the shear in the second layer is nearly at right angles to the low-level shear. None of the rainbands found in this set of experiments is very intense or long-lived.

In the set of experiments labeled 55A in Table 6, the shear in the lower layer is close to its optimal value, and the second layer is of the same thickness and contains the same magnitude shear as the lower layer. As is clear in Fig. 11, the second layer of shear has a dramatic effect on the organization and intensity of convection. If the direction of the shear is the same in both layers (equivalent to doubling the depth of a single shear

TABLE 6. Two-layer shear experiments.

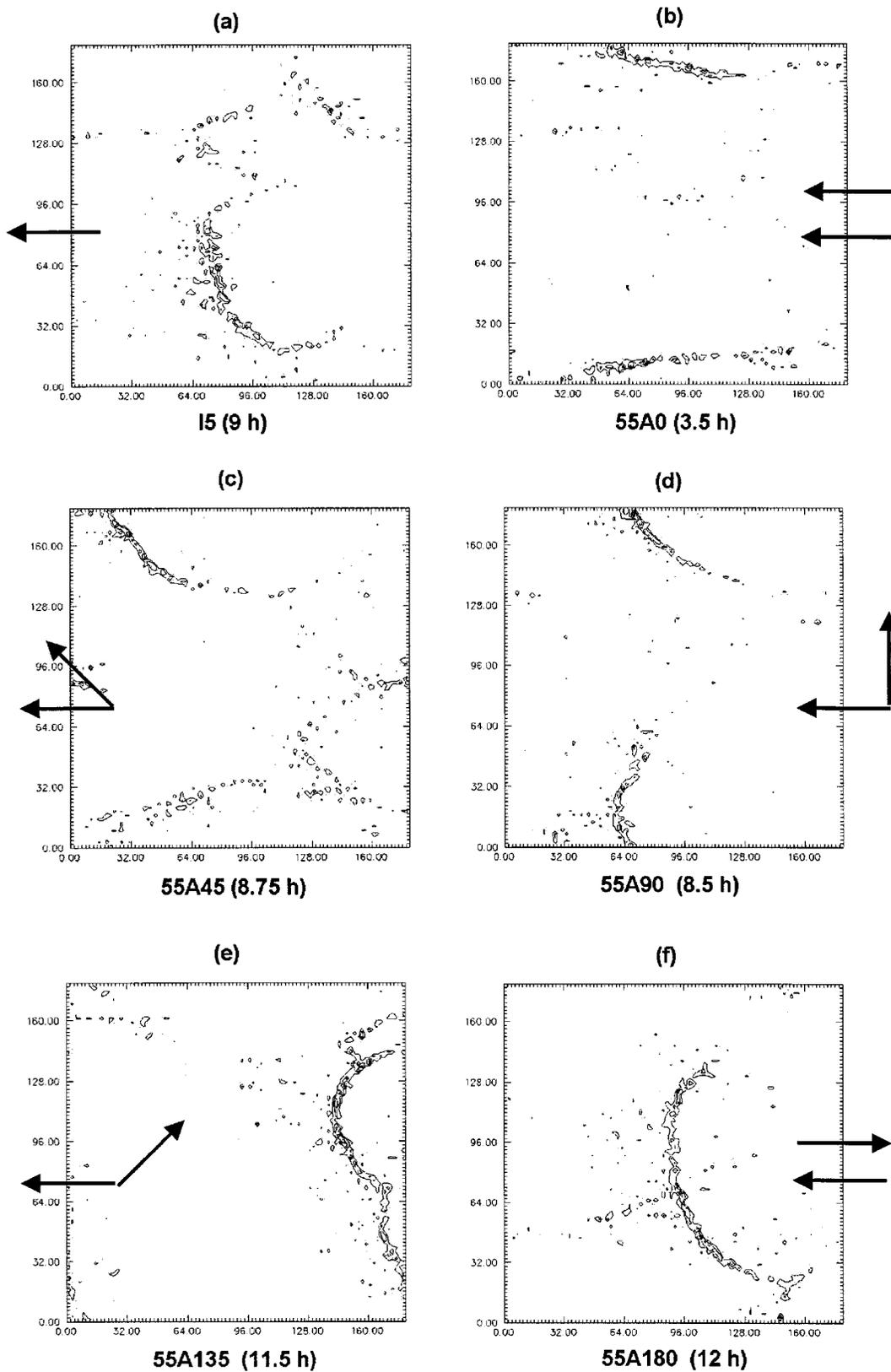| Type	Name	Layer 1 shear (10^{-3} s^{-1})	Layer 2 shear (10^{-3} s^{-1})	Layer 1 thickness (km)	Layer 2 thickness (km)	Orientation angle (thickness)
Orientation						
33a	33A30	3	3	2	2	30
	33A90	3	3	2	2	90
	33A135	3	3	2	2	135
	33A180	3	3	2	2	180
55A	55A0	5	5	2	2	0
	55A45	5	5	2	2	45
	55A90	5	5	2	2	90
	55A135	5	5	2	2	135
	55A180	5	5	2	2	180
73A	73A45	7	3	2	2	45
	73A90	7	3	2	2	90
	73A135	7	3	2	2	135
	73A180	7	3	2	2	180
75A	75A45	7	5	2	2	45
	75A90	7	5	2	2	90
	75A135	7	5	2	2	135
	75A180	7	5	2	2	180
Intensity (S2)	33A90	3	3	2	2	90
	35A90	3	5	2	2	90
	53A180	5	3	2	2	180
	55A180	5	5	2	2	180
H2	33T1	3	3	2	1	90
	33T2	3	3	2	2	90
	33T3	3	3	2	3	90
Constant $\Delta U2$	54T1	5	4	2	2.5	180
	55T2	5	5	2	2	180

FIG. 11. Updraft field at 250 m at selected times in experiments with two layers in shear, varying only the angle between the shear vectors of each layer, which are shown at outer sides of panels. The magnitude of the shear in each layer is 5×10^{-3} s^{-1}. Typical squall lifetimes are indicated by numbers in parentheses below each panel.
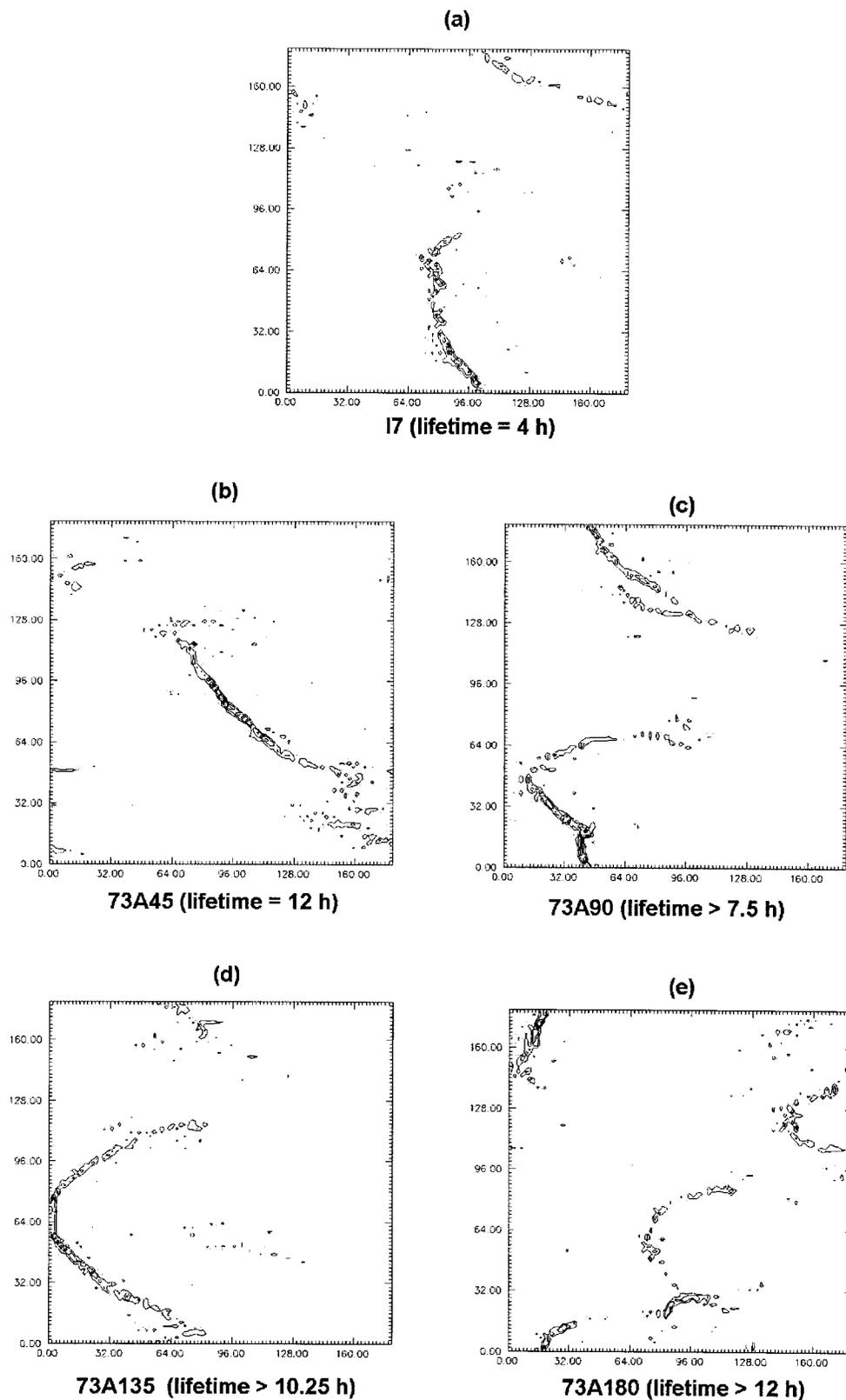
FIG. 12. Same as in Fig.11 except that the magnitude of the shear in the lower layer has been reduced to 3 $\times$ 10^{-3} s^{-1}, while that of the upper layer has been increased to 7 $\times$ 10^{-3} s^{-1}.
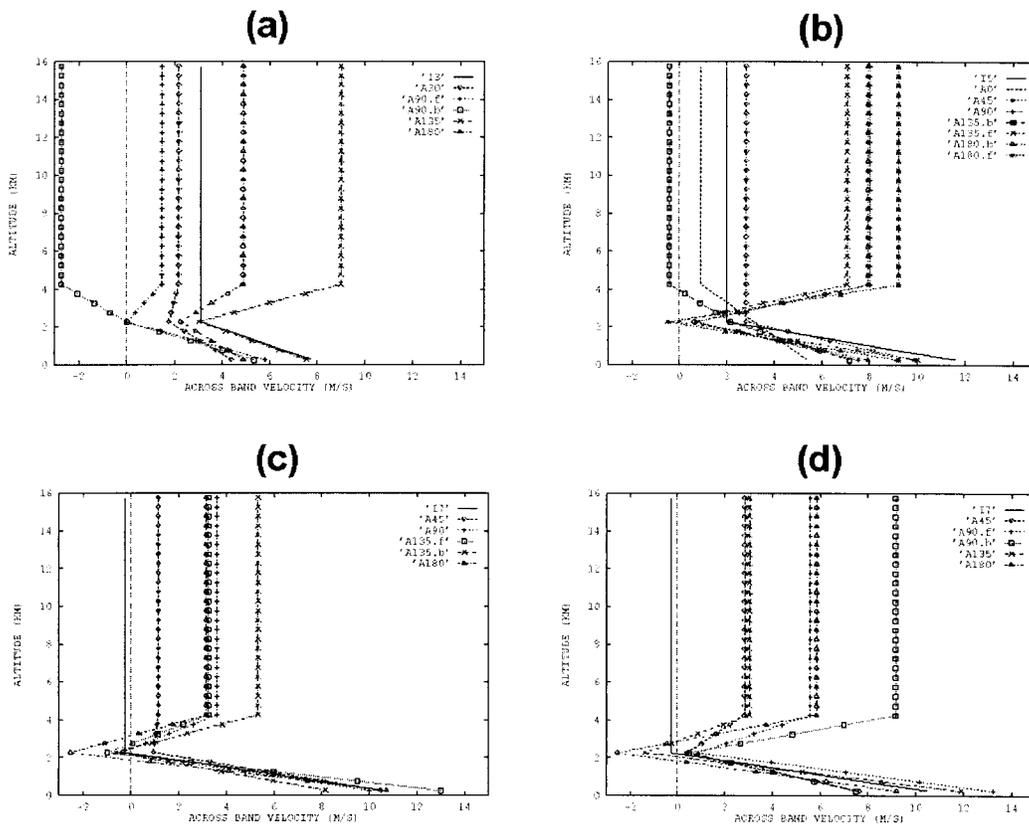
FIG. 13. Band-normal background wind profiles in coordinate systems moving with the bands. Positive values indicate front-to-rear flow. The experiment number (see Tables 1 and 6) is indicated at the upper right of each panel. The suffixes b and f refer, respectively, to profiles relative to the arched-back and front portions of bands. The shear magnitudes in the lower and upper layers are (a) 3×10^{-3} s^{-1} and 3×10^{-3} s^{-1}, (b) 5×10^{-3} s^{-1} and 5×10^{-3} s^{-1}, (c) 7×10^{-3} s^{-1} and 3×10^{-3} s^{-1}, and (d) 7×10^{-3} s^{-1} and 5×10^{-3} s^{-1}.

layer), shear-parallel lines occur. In general, when the angle between the two shear vectors is less than 90°, the convection is weaker and less well organized than in the absence of the second shear layer. As the angle increases beyond 90°, the updrafts become more intense, the cold pools are colder, and the lines are longer lived.

When the magnitude of the lower-layer shear is sufficiently large (experiment set 73A, Table 6), the addition of a second shear layer leads to more intense and better organized convection for all angles between the shear vectors of the two layers. In Fig. 12 it is evident that at small relative angles, lines tend to form parallel to the shear in the second layer. When the second layer shear is directed 180° from the low-layer shear, well-organized arcs of convection occur.

Increasing the magnitude of the shear in the second layer by 65%, while holding the lower-layer shear fixed at its value in experiment set 73A, leads to even stronger squall lines (not shown here). Except when α is 180°, the squall lines tend to be aligned with the second layer shear in this case; when α is 180°, the squall lines are very strong and straight, oriented across the shear.

The propagation of the squall lines relative to the background environmental wind is summarized in Fig.

13, which shows the band-relative (imposed) environmental background flow. To construct Fig. 13, we estimated the orientation of the bands at their mature stage and their motion relative to the ground. In some cases, we also calculated the flow relative to intense, swept-back portions of convective arcs; these are denoted by the suffix b in Fig. 13.

As has been found for a large class of observed squall lines, the flow at almost all levels is from front to back. For the cases with stronger jet profiles, rear-to-front environmental flow is present near 2-km altitude; this may be compared to Barnes and Sieckman's observation that line-relative flow is from front to rear at all level except for a shallow layer just below 4 km. We note, however, that the three-dimensional nature of virtually all bands precludes a simple association between the imposed environmental background flow and the horizontal flow in the vicinity of the squall lines themselves. Indeed, cross sections through individual squall lines or arcs in our experiments show all of the main features that are by now familiar components of squall line circulation, including descending rear inflow jets and strong rear-to-front flow just behind the gust front in the lowest 3–4 km.
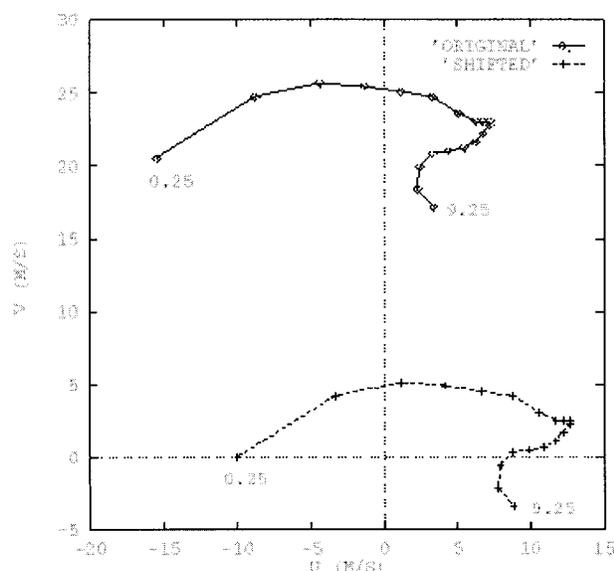
FIG. 14. Wind hodograph observed in the outer region of Hurricane Josephine of 1984 (Powell 1990). Solid line indicates observed hodograph, while dashed line shows hodograph shifted by a Galilean transformation designed to prevent excessively fast propagation of squall lines. The abscissa shows the component of wind across the observed bands, with negative values indicating radially inward flow; the ordinate shows the component of wind along the observed bands.

5. Hurricane outer rainbands

Outside the eyewall(s), convection in tropical cyclones is usually organized into spiral bands, which are a prominent feature of satellite and radar imagery of such storms. Convection in outer hurricane rainbands is not as intense or as continuous as eyewall convection, but rather has a distinctly cellular character similar to that of tropical squall lines (Barnes et al. 1983). Unlike eyewalls, outer bands are not usually associated with wind maxima (Jorgensen 1984; Samsury and Zipser 1995). Their deep convective leading edge is typically 25 km wide, but can be as wide as 80 km (Ryan et al. 1992). As with other tropical squall lines, outer rainbands are associated with cool outflows, whose leading edge is the site of prominent updrafts (Barnes et al. 1983; Barnes and Stossmeister 1986). As with many squall lines, outer hurricane rainbands tend to be oriented at right angles to the low-level shear (Powell 1990a,b; Ryan et al. 1992). They are observed to be nearly stationary with respect to the (translating) vortex but may move slowly radially inward or outward.

Powell (1990a,b) observed that the major differences between outer hurricane rainbands and tropical squall lines are associated with the propagation and structure of their leading and trailing edges. The hurricane rainband downdrafts spread at the surface and apparently help maintain the updrafts; however, they are too weak to propagate into the strong inflow and are thus swept back into a shallow flow on the rear (inner) side of the bands. There is some evidence that, in contrast to most

squall lines, individual cells form at the rear edge and mature at the leading edge of the lines.

Many theories of hurricane spiral rainbands have been advanced. The proposed mechanisms include inertia–gravity waves propagating outward from the eyewall (Tepper 1958; Senn and Hiser 1959), convergence patterns induced by surface friction acting on a translating vortex (Kessler and Atlas 1965; Tatehira 1961; Shapiro 1983), Ekman layer instability (Fung 1977), and shedding of potential vorticity filaments from asymmetries in the inner core (Guinn and Schubert 1993). Here we add to this impressive list by suggesting that outer bands are merely tropical squall lines in the particular kinematic environment of tropical cyclones.

To test this idea, we perform a simulation using a hodograph observed in the outer region of a particular storm, but with all other features identical to those of the simulations described in sections 3 and 4. There are several serious limitations to this approach, for example:

- The thermodynamic profile of hurricanes hardly represents that of radiative–convective equilibrium. In particular, the soundings in the regions where bands are observed are somewhat moister than those obtained in our simulations, owing to much larger surface fluxes and, probably, mean ascent.
- Horizontal variability of the mean flow cannot be easily accounted for owing to the doubly periodic boundary conditions used here. Radial shear of the horizontal wind and flow curvature may both be expected to influence the mesoscale dynamics of rainbands, but these effects are omitted here.

With these limitations in mind, we present the results of a statistical equilibrium simulation using a background hodograph taken from hurricane Josephine (1984), whose outer bands were studied extensively by Powell (1990a,b). This band-relative hodograph is shown in Fig. 14 and extends only to a little more than 9-km altitude, omitting much of the outflow layer. Here, the y axis is oriented along the band; in reality, the band discussed by Powell (1990a,b) was oriented very nearly in the azimuthal direction with respect to the storm center. There is strong low-level vertical shear across the band, averaging around 8.5×10^{-3} s^{-1} up to 2 km.

Representative snapshots of the low-level vertical velocity and surface potential temperature distributions are shown in Fig. 15. The bands that form in these simulations propagate quite rapidly downshear, unlike the observed bands. Their orientation varies over the course of their evolution; the angle between their orientation and the shear vector reaches a maximum value of about 50° at maximum intensity, in comparison with an observed angle of closer to 75°. The cold pool is swept back toward the inner side, as observed, and while the orientation is not that close to the band observed in this storm, it is not dissimilar to the orientation of many observed spiral bands. The cold pool is colder than observed, perhaps owing to the drier sounding in our sim-
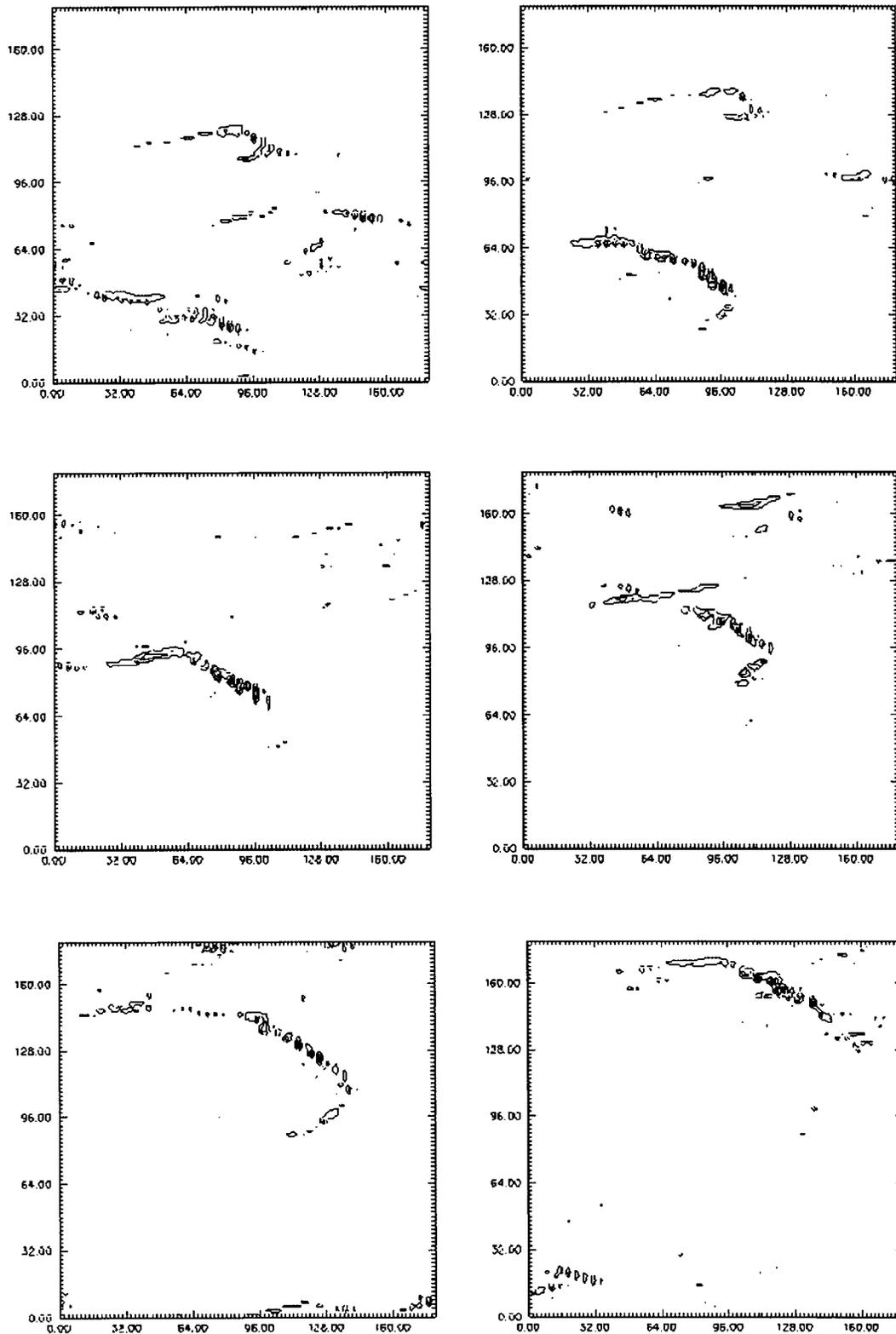
FIG. 15. Updraft field at 250 m in the experiment using the hodograph shown in Fig. 14. The panels show the updraft fields every hour between 6.75 h and 11.75 h, read from left to right and top to bottom.

ulations, and the combination of this and the smaller orientation angle gives overly fast movement of the bands.

We regard these limited simulations as inconclusive so far as our hypothesis is concerned, but at the same time believe that these results warrant an extension to this approach containing a more accurate account of the actual thermodynamic and kinematic environment of outer hurricane rainbands, including a moister sounding and horizontally varying mean flow.

6. Summary

We have undertaken a systematic examination of the effect of background vertical wind shear on the structure and propagation of mesoscale convective systems in a statistical state of radiative–convective equilibrium, and also examined the effect of the shear on the thermodynamic characteristics of the equilibrium state. This work extends previous studies of mesoscale convection by examining equilibrium states in which the form of the convection has become independent of the initial condition. As found in previous studies, low-level shear promotes mesoscale organization into arcs broadly aligned across the shear. The optimum thickness of the shear layer is comparable to the depth of the cold pools formed by downdrafts, as found by RKW, and the optimum value of the shear varies with factors that control the density surfeit of the cold pools. Superoptimal shear promotes the development of lines skewed with respect to the shear, so that the cross-line component of shear is near its optimal value.

We also extended previous work by examining the effects of shear at higher altitudes. Shear at any altitude in the convective layer apparently has some effect on convective organization. Jet profiles, in which the shear direction reverses across the jet level, promote especially strong mesoscale organization. We speculate that the reversed shear flow participates in convective downdrafts, and that the ambient vorticity of this air contributes positively to the downdraft dynamics the same way that the vorticity of the low-level inflow contributes to the updraft dynamics. Strong shear at middle and upper levels, with weak low-level shear, promotes shear-parallel squall lines.

The momentum flux by the convection in shear is nonlocal and can be crudely modeled using Eq. (1) as long as the horizontal momentum within the convective drafts is modeled as in Eq. (2). Assuming conservation of horizontal momentum within the clouds leads, by contrast, to serious overestimates of the convective momentum flux in the case we examined, but it seems very likely that the degree of momentum conservation in the clouds depends on the shape of the hodograph and on the component of horizontal momentum in question.

Shear changes the relative humidity just above the boundary layer and the amount of CAPE in concert, as predicted by the CAPE theory of Emanuel and Bister (1996). With small low-level shear, CAPE increases and low-level relative humidity decreases with shear, while these trends both reverse at higher magnitudes of shear. We do not purport to completely understand the reasons for this behavior, but, as suggested by a reviewer, this may have to do with artificially deep boundary layers created by mechanical turbulence generated by shear in cases where the latter is strong.

It is clear that in many of our simulations, only one mesoscale system exists in the domain at any given time. This suggests that the domain we used is too small in these cases. As computational capacity increases, future work ought to use larger domains in which other modes of self-organization may become apparent. Also, the presence of ice may have a large influence on the extent and duration of anvil systems and may thus have a noticeable effect on the behavior of mesoscale convective systems; this ought to be explored in future work.

REFERENCES

Barnes, G. M., and K. Sieckman, 1984: The environment of fast- and slow-moving tropical mesoscale convective cloud lines. *Mon. Wea. Rev.,* **112,** 1782–1794.
——, and G. J. Stossmeister, 1986: The structure and decay of a rainband in Hurricane Irene (1981). *Mon. Wea. Rev.,* **114,** 2590–2601.
——, E. J. Zipser, D. Jorgensen, and F. Marks, 1983: Mesoscale and convective structure of a hurricane rainband. *J. Atmos. Sci.,* **40,** 2125–2137.
Dudhia, J., M. W. Moncrieff, and D. W. K. So, 1987: The two-dimensional dynamics of West African squall lines. *Quart. J. Roy. Meteor. Soc.,* **113,** 121–146.
Emanuel, K. A., 1986: Some dynamical aspects of precipitating convection. *J. Atmos. Sci.,* **43,** 2183–2198.
——, and M. Bister, 1996: Moist convective velocity and buoyancy scales. *J. Atmos. Sci.,* **53,** 3276–3285.
——, and M. Zivkovic-Rothman, 1999: Development and evaluation of a convection scheme for use in climate models. *J. Atmos. Sci.,* **56,** 1766–1782.
Fovell, R. G., and Y. Ogura, 1988: Numerical simulation of a midlatitude squall line in two dimensions. *J. Atmos. Sci.,* **45,** 3846–3879.
——, and ——, 1989: Effect of vertical wind shear on numerically simulated multicell storm structure. *J. Atmos. Sci.,* **46,** 3144–3176.
Fung, I. Y.-S., 1977: The organization of spiral rain bands in a hurricane. Ph.D. dissertation, Massachusetts Institute of Technology, 139 pp. [Available from Department of Earth, Atmospheric and Planetary Science, MIT, 77 Mass. Ave., Cambridge, MA 02139.]

Guinn, T. A., and W. H. Schubert, 1993: Hurricane spiral bands. *J. Atmos. Sci.,* **50,** 3380–3403.

Hane, C. E., 1973: The squall line thunderstorm: Numerical experimentation. *J. Atmos. Sci.,* **30,** 1672–1690.

Islam, S., 1991: Predictability of mesoscale precipitation. Sc.D. dissertation, Massachusetts Institute of Technology, 240 pp. [Available from the Department of Civil Engineering, MIT, 77 Mass. Ave., Cambridge, MA 02139.]

——, R. L. Bras, and K. A. Emanuel, 1993: Predictability of mesoscale rainfall in the Tropics. *J. Appl. Meteor.,* **32,** 297–310.

Jordan, C. L., 1958: Mean soundings for the West Indies area. *J. Meteor.,* **15,** 91–97.

Jorgensen, D. J., 1984: Mesoscale and convective-scale characteristics of mature hurricanes. Part I: General observations by research aircraft. *J. Atmos. Sci.,* **41,** 1268–1285.

Kershaw, R. and D. Gregory, 1997: Parametrization of momentum transport by convection. Part 1. Theory and cloud modelling results. *Quart. J. Roy. Meteor. Soc.,* **123,** 1133–1151.

Kessler, E., 1969: *On the Distribution and Continuity of Water Substance in Atmospheric Circulation.* American Meteorological Society, 84 pp.

——, and D. Atlas, 1965: Radar synoptic analysis of Hurricane Edna. Geophysical Research Papers, No. 50, 113 pp. [Available from Air Force Cambridge Research Center, Hanscom Air Force Base, Bedford, MA 01730.]

Lafore, J. P., and M. W. Moncrieff, 1989: A numerical investigation of the organization and interaction of the convective and stratiform regions of tropical squall lines. *J. Atmos. Sci.,* **46,** 521–544.

Mapes, B. E., and X. Wu, 2001: Convective eddy momentum tendencies in long cloud-resolving model simulations. *J. Atmos. Sci.,* **58,** 517–526.

Nicholls, M. E., 1987: A comparison of the results of a two-dimensional numerical simulation of a tropical squall line with observations. *Mon. Wea. Rev.,* **115,** 3055–3077.

——, and M. J. Weissbluth, 1988: A comparison of two-dimensional and quasi-three-dimensional simulations of a tropical squall line. *Mon. Wea. Rev.,* **116,** 2437–2452.

Powell, M. D., 1990a: Boundary layer structure and dynamics in outer hurricane rainbands. Part I: Mesoscale rainfall and kinematic structure. *Mon. Wea. Rev.,* **118,** 891–917.

——, 1990b: Boundary layer structure and dynamics in outer hurricane rainbands. Part II: Downdraft modification and mixed layer recovery. *Mon. Wea. Rev.,* **118,** 918–938.

Robe, F. R., 1996: Sea, sun and shear: A recipe for precipitating convection, tropical rainbands, and hurricane spiral arms. Ph.D. dissertation, Massachusetts Institute of Technology, 242 pp. [Available from the Department of Earth, Atmospheric and Planetary Science MIT, 77 Mass. Ave., Cambridge, MA 02139.]

——, and K. A. Emanuel, 1996: Dependence of tropical convection on radiative forcing. *J. Atmos. Sci.,* **53,** 3265–3275.

Rotunno, R., J. B. Klemp, and M. L. Weisman, 1988: A theory for strong, long-lived squall lines. *J. Atmos. Sci.,* **45,** 463–485.

Ryan, B. F., G. M. Barnes, and E. J. Zipser, 1992: A wide rainband in a developing tropical cyclone. *Mon. Wea. Rev.,* **120,** 431–447.

Samsury, C. E., and E. J. Zipser, 1995: Secondary wind maxima in hurricanes: Airflow and relationship to rainbands. *Mon. Wea. Rev.,* **123,** 3502–3517.

Schlesinger, R. E., 1973: A numerical model of deep moist convection: Part I. Comparative experiments for variable ambient moisture and wind shear. *J. Atmos. Sci.,* **30,** 835–856.

Schneider, E. K., and R. S. Lindzen, 1976: A discussion of the parameterization of momentum exchange of cumulus convection. *J. Geophys. Res.,* **81,** 3158–3160.

Senn, H. V., and H. W. Hiser, 1959: On the origin of hurricane spiral rainbands. *J. Meteor.,* **16,** 419–426.

Shapiro, L. J., 1983: The asymmetric boundary-layer flow under a translating hurricane. *J. Atmos. Sci.,* **40,** 1984–1998.

Skamarock, W. C., M. L. Weisman, and J. B. Klemp, 1994: Three-dimensional evolution of simulated long-lived squall lines. *J. Atmos. Sci.,* **51,** 2563–2584.

Takeda, T., 1971: Numerical simulation of a precipitating convective cloud: The formation of a ''long-lasting'' cloud. *J. Atmos. Sci.,* **28,** 350–376.

Tatehira, 1961: A mesoscale and radar analysis of typhoon rainband, case study of Typhoon Helen, 1958. *Proc. Second Tech. Conf. on Hurricanes,* Miami Beach, FL, Amer. Meteor. Soc., 115–126.

Tepper, M., 1958: A theoretical model for hurricane radar bands. Preprints, *Seventh Conf. on Radar Meteorology,* Boston, MA, Amer. Meteor. Soc., K56–K65.

Thompson, S. L., and S. G. Warren, 1982: Parameterization of outgoing infrared radiation derived from detailed radiative calculations. *J. Atmos. Sci.,* **39,** 2667–2680.

Thorpe, A. J., M. J. Miller, and M. W. Moncrieff, 1982: Two-dimensional convection in non-constant shear: A model of midlatitude squall lines. *Quart. J. Roy. Meteor. Soc.,* **108,** 739–762.

Trier, S. B., W. C. Skamarock, and M. A. LeMone, 1997: Structure and evolution of the 22 February 1993 TOGA COARE squall line: Organization mechanisms inferred from numerical simulation. *J. Atmos. Sci.,* **54,** 386–407.

Vallis, G. K., G. J. Shutts, and M. E. B. Gray, 1997: Balanced mesoscale motion and stratified turbulence forced by convection. *Quart. J. Roy. Meteor. Soc.,* **123,** 1621–1652.

Weisman, M. L., 1993: The genesis of severe, long-lived bow echoes. *J. Atmos. Sci.,* **50,** 645–670.

Wyss, J., and K. A. Emanuel, 1988: The pre-storm environment of midlatitude prefrontal squall lines. *Mon. Wea. Rev.,* **116,** 790–794.

Xue, M., K. K. Droegemeier, V. Wong, A. Shapiro, and K. Brewster, 1993: Advanced Regional Prediction System, Version 3.1 user's guide. 186 pp. [Available from the Center for Analysis and Prediction of Storms, University of Oklahoma, Norman, OK, 73019.]

Yoshizaki, M., 1986: Numerical simulations of tropical squall-line clusters: Two-dimensional model. *J. Meteor. Soc. Japan,* **64,** 469–491.